

Effects of Ni Substitutions on the Critical Behaviors in $\text{Nd}_{0.6}\text{Sr}_{0.4}\text{Mn}_{1-x}\text{Ni}_x\text{O}_3$

Manganite.

M. Kh. Hamad^{a*}, Y. Maswadeh^b, and Kh. A. Ziq^a

^aPhysics Department, King Fahd University of Petroleum and Minerals. Dhahran, 31261, Saudi Arabia.

^bDepartment of Physics and Science of Advanced Materials Program, Central Michigan University, Mt. Pleasant, Michigan 48859, United States.

ABSTRACT

We investigate the effect of Ni-substitution on the crystalline structure and the critical behavior of $\text{Nd}_{0.6}\text{Sr}_{0.4}\text{Mn}_{1-x}\text{Ni}_x\text{O}_3$ ($0.00 \leq x \leq 0.20$) perovskite. X-ray diffraction patterns revealed that the major phase in all samples is the orthorhombic structure with space group *Pnma*. Rietveld refinement revealed a linear reduction in the lattice parameters along with monotonic reduction in the *O2-Mn-O2* angle with increasing Ni concentration. The modified Arrott plots and the Kouvel-Fisher method have been used to analyze the magnetization isotherms near the paramagnetic to ferromagnetic (PM-FM) phase transition. The obtained critical exponents (β , γ and δ) revealed that the *Ni*-free sample is consistent with 3D-Heisenberg like behavior. However, upon Ni-substitution, the critical exponents exhibit a mean field like behavior. The reliability of the obtained critical exponent (β , γ , and δ) values have been confirmed by the universal scaling behavior of the isothermal magnetization near the transition temperature.

1. INTRODUCTION

The rich magnetic phase diagram often found in manganites arises from the interplay between the spin, orbital, charge, and lattice degrees of freedom. This is reflected in the wide variety in

their properties, such as transport, magnetic, magnetoresistance (MR) and magnetocaloric effect (MCE) [1-4].

Perovskite manganites are generally represented as $R_{1-x}A_xMnO_3$, where R is a rare-earth element such as $Nd, La, \text{ and } Ce$, and A is a divalent alkaline earth metal like $Sr, Ca, Ba, \text{ and } etc.$ These materials undergo a combination of several phases: metallic, insulating, and various magnetic phases; ferromagnetic, ferrimagnetic, antiferromagnetic and spin-glass [5]. The level of substitution with a divalent alkaline earth metal in these manganites affects the exchange interaction, revealing a wide variation in many physical properties like the magnetoresistance (MR) and magnetocaloric effect (MCE) [6]. Moreover, the paramagnetic to ferromagnetic phase transition and the corresponding critical exponents near the transition temperature is expected to be affected by these substitutions.

The critical exponents are commonly evaluated using the isothermal magnetization along with Kouvel-Fisher procedure [7, 9-10]. However, for various perovskite manganites there is a wide discrepancy in the reported values of the critical exponents covering the range between the short-range Heisenberg model ($\beta = 0.365, \gamma = 1.336, \text{ and } \delta = 4.800$) to the long-range mean-field theory ($\beta = 0.5, \gamma = 1, \text{ and } \delta = 3$). These variations may be related to differences in the micro-structure and possible disorder effects caused by variations in the preparation methods [4, 8].

The phase diagram of $Nd_{1-x}Sr_xMnO_3$ perovskite reveals a variety of magneto-electric properties [11]. Near $x = 0.4$, the material is insulating ferromagnet with maximum Curie temperature $T_c \sim 300K$ and maximum saturated magnetization. These properties lend the material attractive in near room temperature magnetocaloric cooling, sensing devices and data storage applications [12-13]. Moreover, the effects of transition metal substitutions on various magnetic states and their critical behavior has received little attention in this system.

In this paper, we investigate the effects of Ni-substitutions on the critical exponents in $\text{Nd}_{0.6}\text{Sr}_{0.4}\text{Mn}_{1-x}\text{Ni}_x\text{O}_3$ ($0.00 \leq x \leq 0.20$) polycrystalline samples near its FM-PM phase transition. The corresponding critical exponents are determined from the modified Arrott plots [9] and are confirmed by Kouvel-Fisher method [10]. The obtained critical exponents revealed that the unsubstituted sample $\text{Nd}_{0.6}\text{Sr}_{0.4}\text{MnO}_3$ is consistent with 3D-Heisenberg like behavior. Upon Ni-substitution, the critical exponents exhibit a mean field like behavior. The obtained critical exponent (β , γ , and δ) have been used to generate the universal scaling behavior of the isothermal magnetization near the transition temperature.

2. EXPERIMENTAL DETAILS

The polycrystalline $\text{Nd}_{0.6}\text{Sr}_{0.4}\text{Mn}_{1-x}\text{Ni}_x\text{O}_3$ ($0 \leq x \leq 0.2$) were prepared using a standard solid-state reaction. Stoichiometric ratios of high purity (4N) oxides (Nd_2O_3 , SrCO_3 , MnO_2 , and NiO) were used to prepare the samples. The oxides were mixed and grinded for about 30 minutes. The resulting powder was calcinated in the air for 24 hours at 1000°C . The samples were re-grinded, pressed and re-annealed at 1000°C and 1300°C for 10 hours. The last step was repeated one more time and the samples were furnace cooled to room temperature. Powder x-ray diffraction patterns were obtained using Bruker XRD (Phaser D2 2nd-G) with $\text{Cu K}\alpha$ ($\lambda=1.54056 \text{ \AA}$). The crystalline structure was analyzed in the range $20\text{-}80^\circ$ using Rietveld refinements available in FULLPROF software. VESTA and Diamond software [14-15] were used to determine the atomic distances and angles between Mn ion and the nearest oxygen ions neighbors. The analyses included the refined crystal parameters, the secondary phases, and the cationic distributions in the lattice [16].

A homemade ac -susceptometer was fitted inside a Janis closed cycle refrigerator (model SHI-4T). The susceptometer was used to monitor the variation of the susceptibility with temperature in the temperature range (4 to 325K). LABVIEW software is used to control the lock-in-amplifier

(SR850) and the Lake Shore 336 temperature controller. The Magnetization measurements were performed using a 9-Tesla PAR-Lakeshore (Model 4500/150A) vibrating sample magnetometer (VSM).

3. RESULTS AND ANALYSIS

3.1 X-ray Diffraction analysis (XRD)

A representative of the XRD patterns for $Nd_{0.6}Sr_{0.4}Mn_{1-x}Ni_xO_3$ for $x = 0.00$ and $x = 0.05$ along with Rietveld refinement [17, 18] are shown in Fig.1.

The results of the refinement revealed that the orthorhombic structure as the major phase in all samples ($Nd_{0.6}Sr_{0.4}Mn_{1-x}Ni_xO_3$) with $Pnma$ (62) space group. A minor cubic perovskite phase with space group $Pm\bar{3}m$ (221) has also been detected in all samples. Venkatesh *et al.* reported the presence of pseudocubic phase in $Nd_{0.67}Sr_{0.33}MnO_3$ sample and the orthorhombic phase in $Nd_{0.6}Sr_{0.4}MnO_3$; however, no details were given about heat treatment [12]. Abdel-Latif *et al* used chemical co-precipitation method and low annealing temperature (850 °C) to produce pure orthorhombic phase of $Nd_{0.6}Sr_{0.4}MnO_3$ [19-20]. Moreover, Mansour *et al* used high temperature annealing (1200~1300 °C) to prepare $Nd_{0.6}Sr_{0.4}MnO_3$, they obtained almost pure orthorhombic phase with traces of the cubic phase [13].

We performed the refined lattice parameters, unit cell volume, and reliability (R) factors for both phases. The results are listed in Table 1 and in figures 2. We report specifically the R_f -factor and the Bragg R_B -factor; these factors are referring to the crystallographic agreement and the reflected intensities agreement consecutively. The values of these factors (Table 1) indicate a very good agreement between the XRD patterns and the reflected intensities generated by the space groups.

The results (Table 1) shown in Fig. 2 indicates almost linear reduction in the lattice parameters (a , b , and c), and the unit cell volume (V) with increasing Ni concentration. The reduction in the lattice parameters is consistent with the smaller ionic radius of Ni as compared to Mn ionic radius [21-22]. Upon Ni-substitution at the Mn site, the (200) peak (inset to figure 1) shifts towards higher angles. This indicates a gradual reduction in the lattice parameter (a) (Table 1) which is in line with the observed shortening in the $Mn-O$ bonds (Table 2). Moreover; this is consistent with a slight increase in the concentration of the smaller Mn^{4+} ions (0.530\AA) and decrease in the concentration of the larger Mn^{3+} ions (0.645\AA) [23]. This is further supported by the slight decrease in the saturated magnetization of sample with higher Ni-concentration -see figure 7.

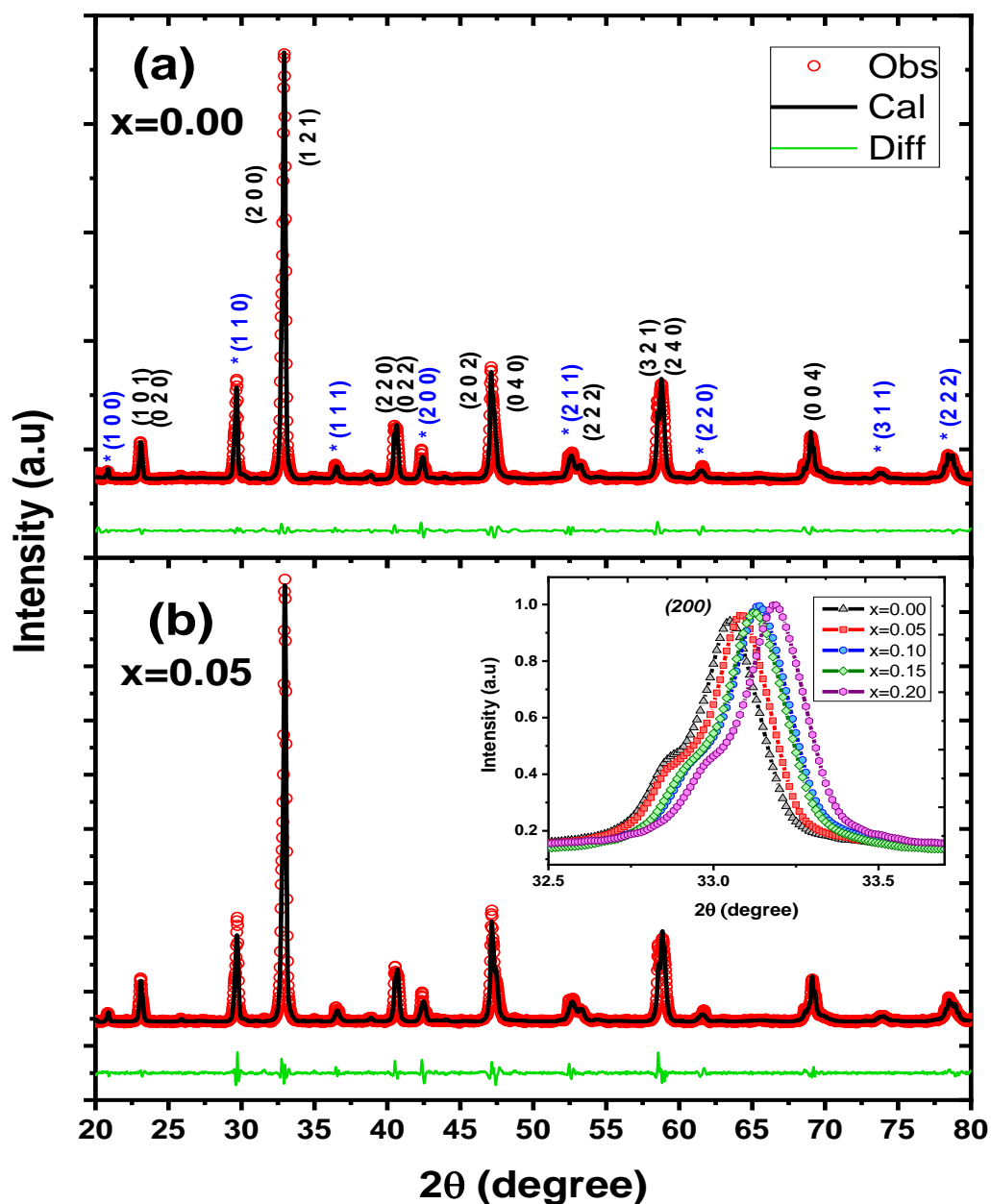


Figure 1: X-ray diffraction patterns for (a) $x = 0.00$, and (b) $x = 0.05$ sample at room temperature. The (hkl) values corresponding to Bragg peaks of primary (in black) and secondary (in blue with stars) phases are marked. The inset shows (200) reflection peaks for different Ni concentration ($0.00 \leq x \leq 0.20$). The diffraction peak is shifted positively in 2θ upon increasing the Ni content in the sample.

The change in lattice parameters leads to changes in the bond lengths ($Mn-O$), and hence the bonds angles ($O-Mn-O$) as shown in Table 2 and figure 3. VESTA software was used to determine the distances ($Mn-O$) between Mn ions and the nearest neighbors of oxygen ions as well as the ($O-Mn-O$) bond angles. The coordination octahedral of Mn is presented in Fig. 4. The Wyckoff positions of ions in the orthorhombic structure are also given (see Table 3).

Table 1: Summary of the refinement of XRD patterns of $Nd_{0.6}Sr_{0.4}Mn_{1-x}Ni_xO_3$ manganites.

Concentration (x)	0	0.05	0.10	0.15	0.20
<i>Phase 1: $Nd_{0.6}Sr_{0.4}Mn_{1-x}Ni_xO_3$</i>		<i>Space group: $Pnma$ (62) – orthorhombic</i>			
$a(\text{Å})$	5.47(0)	5.46(6)	5.46(5)	5.45(8)	5.45(3)
$b(\text{Å})$	7.67(5)	7.66(0)	7.66(0)	7.65(2)	7.64(7)
$c(\text{Å})$	5.43(6)	5.43(1)	5.42(8)	5.42(0)	5.41(4)
$V(\text{Å}^3)$	228.19	227.41	227.23	226.34	225.74
R_B	1.91	2.04	1.5	1.15	2.53
R_F	3.18	2.47	2.27	1.71	2.68
<i>Phase 2: $Nd(Sr)MnO_3$</i>		<i>Space group: $Pm\bar{3}m$ (221) – cubic</i>			
$a(\text{Å})$	4.26(3)	4.25(8)	4.25(7)	4.25(1)	4.24(7)
$V(\text{Å}^3)$	77.45	77.20	77.15	76.82	76.61
R_B	2.38	1.71	2.6	1.94	1.89
R_F	1.87	1.32	1.78	1.28	1.10

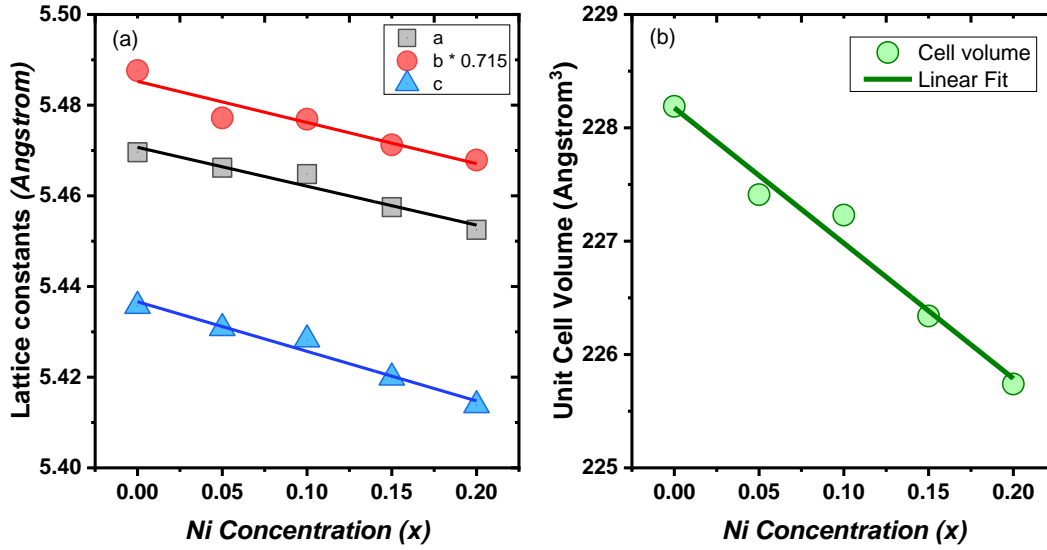


Figure 2: Change of lattice constants and unit cell volume with increasing the Ni fraction.

Table 2: Bonds length and bonds angles of $Nd_{0.6}Sr_{0.4}Mn_{1-x}Ni_xO_3$ manganites.

x	$Mn-O1$ (Å)	$Mn-O2$ (Å)	$Mn-O2$ (Å)	$O1-Mn-O1$ (deg)	$O2-Mn-O2$ (deg)
0.00	1.94(8)	1.95(8)	1.98(9)	180	90.97(5)
0.05	1.93(1)	1.92(4)	1.99(3)	180	90.36(7)
0.10	1.94(6)	1.94(9)	1.96(6)	180	90.05(6)
0.15	1.95(2)	1.93(0)	1.95(7)	180	89.76(5)
0.20	1.92(7)	1.91(7)	1.97(2)	180	89.54(0)

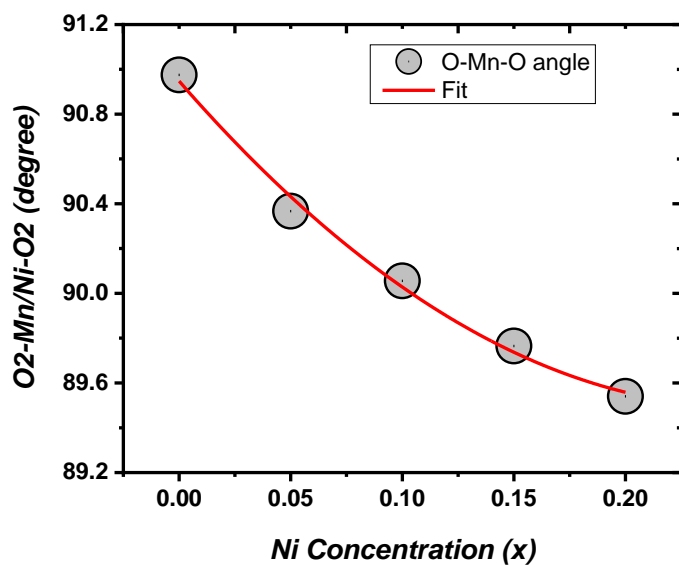


Figure 3: Change of bond angles of $\text{Nd}_{0.6}\text{Sr}_{0.4}\text{Mn}_{1-x}\text{Ni}_x\text{O}_3$ upon Ni concentration.

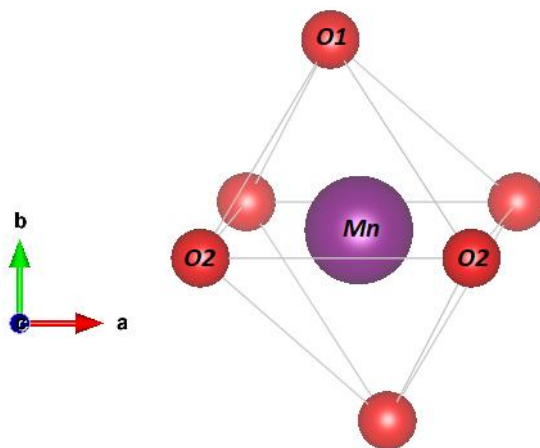


Figure 4: The coordinate of polyhedral of Mn in $\text{Nd}_{0.6}\text{Sr}_{0.4}\text{Mn}_{1-x}\text{Ni}_x\text{O}_3$ compound.

Table 3: Wyckoff positions of ions in the orthorhombic structure for *Pnma* (62) space group.

<i>Pnma</i> (62) - orthorhombic				
Atom	Wyck.	x/a	y/b	z/c
Nd	4c	0.012(5)	0.250(0)	0.005(4)
Sr	4c	0.012(5)	0.250(0)	0.005(4)
Mn	4b	0.0000	0.0000	0.500(0)
O1	4c	0.467(9)	0.250(0)	0.031(7)
O2	8d	0.281(1)	0.027(8)	0.725(7)
Ni	4b	0.0000	0.0000	0.500(0)

Distortion of the ideal perovskite structure is very important parameter since it correlates with magnetic properties. The obtained distortion index (D), quadratic elongation, Octahedrons volume, and bond angle variance are summarized in Table 4. There is no major structural deformation on the MnO_6 octahedron upon Ni concentration, the quadratic elongation values are very close to 1 (1.006 ± 0.003), and the calculated distortion index are very small ($\sim 0.010 \pm 0.005$), which indicates that the calculated structure is in good agreement with the structure of the material. The octahedron volume is decreasing with increasing Ni concentration, consistent with the smaller Ni-ionic radius compared with Mn-ionic radius, further supporting that Ni is substituting Mn 4b site.

Table 4: Octahedral volume, distortion index and quadratic elongation of Mn polyhedral in



X	Octahedral volume (\AA^3)	Distortion index (bond length)	Quadratic elongation
0.00	9.98(7)	0.008(1)	1.00(9)
0.05	9.78(7)	0.015(0)	1.00(7)
0.10	9.85(8)	0.004(3)	1.00(6)
0.15	9.72(0)	0.005(7)	1.00(8)
0.20	9.66(5)	0.011(3)	1.00(4)

3.2 AC-susceptibility

The ac-susceptibility for all samples are measured at 887Hz and the amplitude of the field $H_{ac}=0.10e$. The normalized real part of the susceptibility is presented in Fig. 5a and its derivative in Fig. 5b. The position of the minimum in the derivative is taken as the Curie temperature. Figure 5b reveals a gradual reduction in the transition temperature along with increase in the full-width at half maximum (*FWHM*) with increasing Ni-concentration. The reduction in T_c is presented in Fig. 6, indication linear decrease in T_c . It is worth mentioning that upon increasing the frequency, there is a very small (less than 0.10 K) shift in the peak temperatures over the frequency range (100-5000 Hz) [7].

In Nd-manganites, Nd -ions as Nd^{3+} . However; Mn ions may have several oxidation states mostly: Mn^{4+} , Mn^{3+} and Mn^{2+} . Substitution with Ni^{2+} at the Mn site ultimately affects the charge distribution and the overall magnetic state of the Nd-manganites. This may results in a

reduction of the ferromagnetic transition temperature (T_c) and the associated FM exchange interaction. It also enhances the antiferromagnetic behavior as expected for an oxide material in which the magnetism is mediated by super exchange through the oxygen [24]. The indirect exchange interaction depends on the degree of overlap of orbitals, which in turn is strongly dependent upon the angle of the $Mn - O - Mn$ bond, where the $3d$ electrons delocalized over this bond. This bond is strongly depending upon substitution where Mn^{4+}/Mn^{3+} ratio is affected, and hence interruption of $Mn - O - Mn$ double exchange interaction.

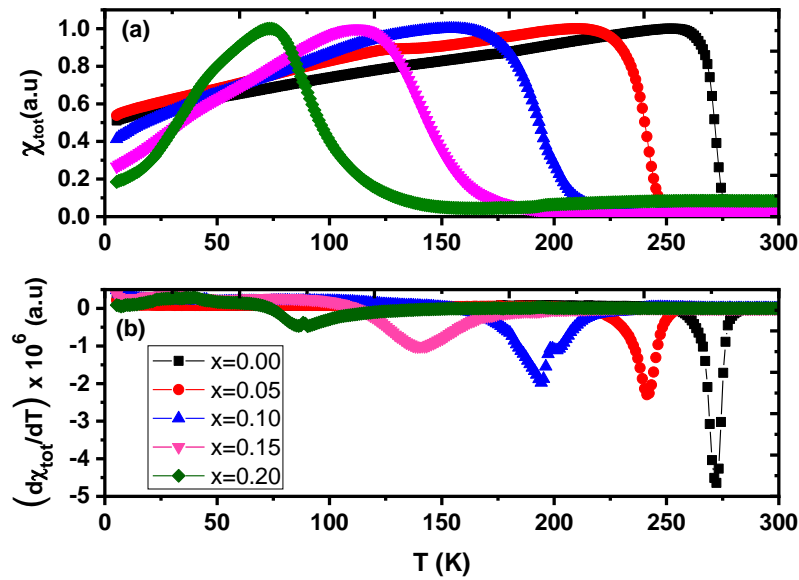


Figure 5: (a) Normalized total ac-susceptibility for $Nd_{0.6}Sr_{0.4}Mn_{1-x}Ni_xO_3$ ($0 \leq x \leq 0.2$) polycrystalline, (b) their first derivative.

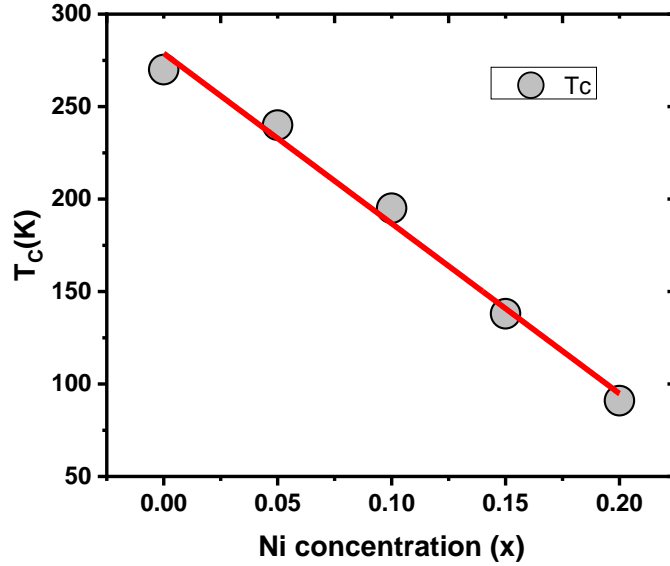


Figure 6: Effect of Ni substitutions on critical temperature in $Nd_{0.6}Sr_{0.4}Mn_{1-x}Ni_xO_3$ compounds.

3.3 The Modified Arrott plot (MAP)

The conventional method to determine the critical exponents and transition temperature involves the use of Arrott plots or the modified Arrott plots along with Kouvel-Fischer plots [9, 10]. In the Arrott plot; the analysis is based on the mean field theory expansion of the free energy. The magnetization isotherms are presented as M^2 vs. H/M . At relatively high fields (few kOe), the analysis leads to a set of parallel straight lines near T_C . At T_C , the magnetic isotherm passes through the origin. Deviations from linearity may persists at the high-field regions, hence reflecting deviations for the mean-field model. Banerjee suggested that the presence of curvature may indication of a second-order phase transition [25].

To accommodate these deviations, one may resort to critical behavior analysis using the modified Arrott-plot (MAP) techniques. This is based on Arrott-Noakes equation of state that holds well in the asymptotic critical region [9].

$$(H/M)^{1/\gamma} = (T - T_c)/T_1 + (M/M_1)^{1/\beta} \quad (1)$$

Here, T_1 and M_1 are constants; γ and β are the critical exponents of the phase transition.

The critical behavior of phase transition has been extensively studied using various theoretical models for the magnetic spin configurations. The commonly used models are: 3D-Heisenberg ($\gamma = 1.336$ and $\beta = 0.365$), the tricritical mean-field ($\gamma = 1$ and $\beta = 0.25$), the 3D-Ising ($\gamma = 1.24$ and $\beta = 0.325$) and the 3D-XY ($\gamma = 1.316$ and $\beta = 0.345$). The third critical exponent δ can be evaluated using the magnetization isotherm at the transition temperature T_c . It can also be calculated from the Widom scaling relation $\delta = 1 + \frac{\gamma}{\beta}$ [26-27].

The modified Arrott analysis is greatly improved using Kouvel-Fisher plots in order to obtain reliable experimental values of the critical exponents.

The magnetization isotherms for all prepared samples are measured in the temperature range 4-300K and in an applied magnetic field 0-5 Tesla. A representative of these measurements is shown in Fig. 7 for temperatures 100K to just above T_c for each sample. The figures revealed a reduction in the saturated magnetization M_s with increasing Ni concentration. Moreover, the high field susceptibility, as obtained from the slope of the magnetization at high fields (~ 4 Tesla) is increasing with increasing Ni contents. This also indicates that samples with high Ni-contents needs higher applied magnetic field to reach saturation. This also indicates strengthening of the antiferromagnetic interaction with increasing Ni-contents.

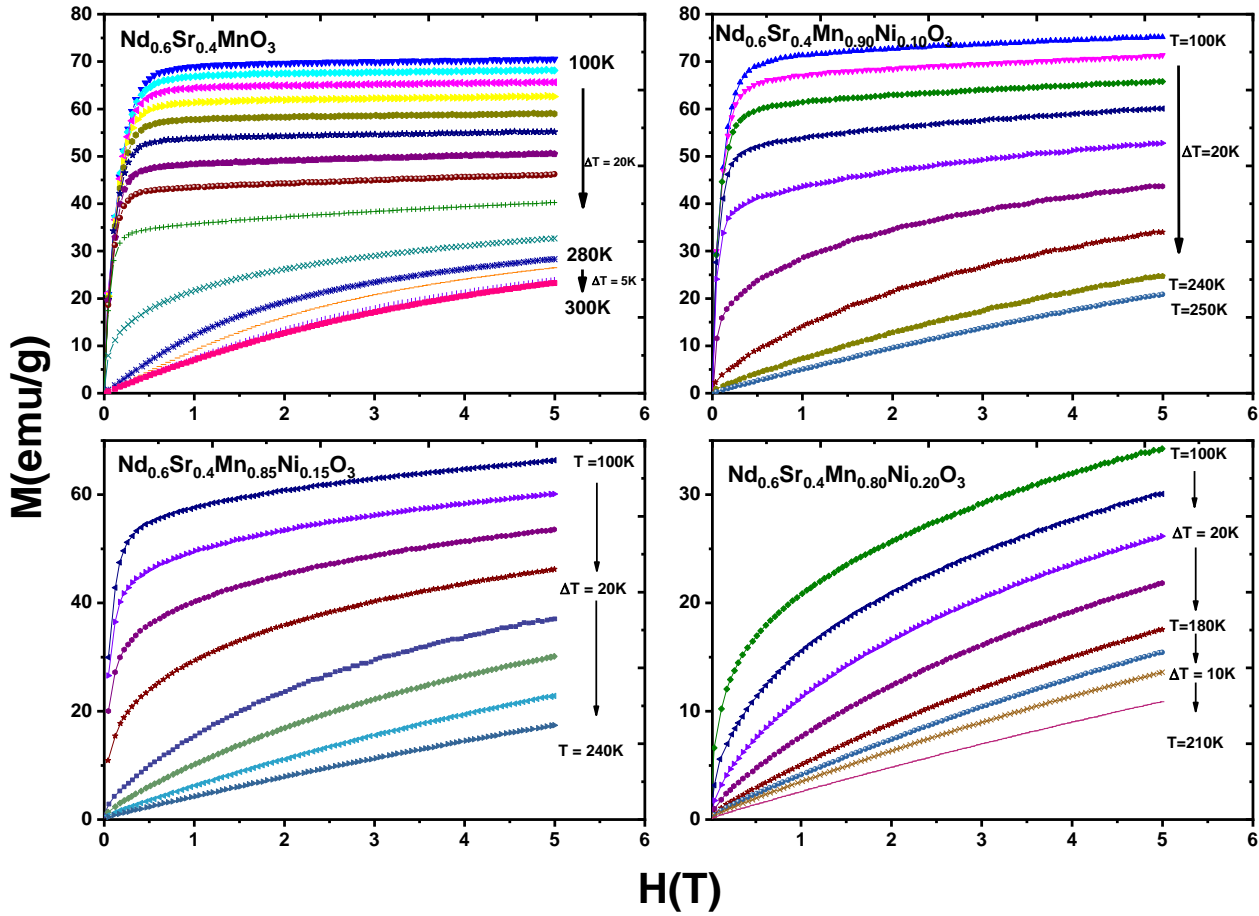


Fig. 7: Magnetic isotherms for $Nd_{0.6}Sr_{0.4}Mn_{1-x}Ni_xO_3$ above 100K.

The magnetic isotherms are represented as $M^{1/\beta}$ vs. $(H/M)^{1/\gamma}$ plots at different temperatures for $x = 0.00$ using four different models (Fig. 8): the 3D-Heisenberg model, the tricritical mean-field models, the 3D-Ising model, and the 3D-XY model. The theoretical values of β , γ and δ for each model are given for example in reference [26-27].

Based on these curves (Fig. 8), all models render quasi-straight lines and nearly parallel at high field (~ 3 Tesla). The slope of these lines relative to the slope at T_c (RS) is used to determine which model closely represents the magnetic state at hand. The variations of RS values -for the various models- with temperature are presented in figure 9. The most adequate model should be

the one with RS curve close to RS=1 [28]. Therefore, one can infer from Fig. 9 that the 3D-Heisenberg model is the nearest to the horizontal line at RS = 1 for $\text{Nd}_{0.6}\text{Sr}_{0.4}\text{MnO}_3$ sample ($x = 0.00$), while for $x = 0.05$, the sample behaves like mean field model (Fig. 9).

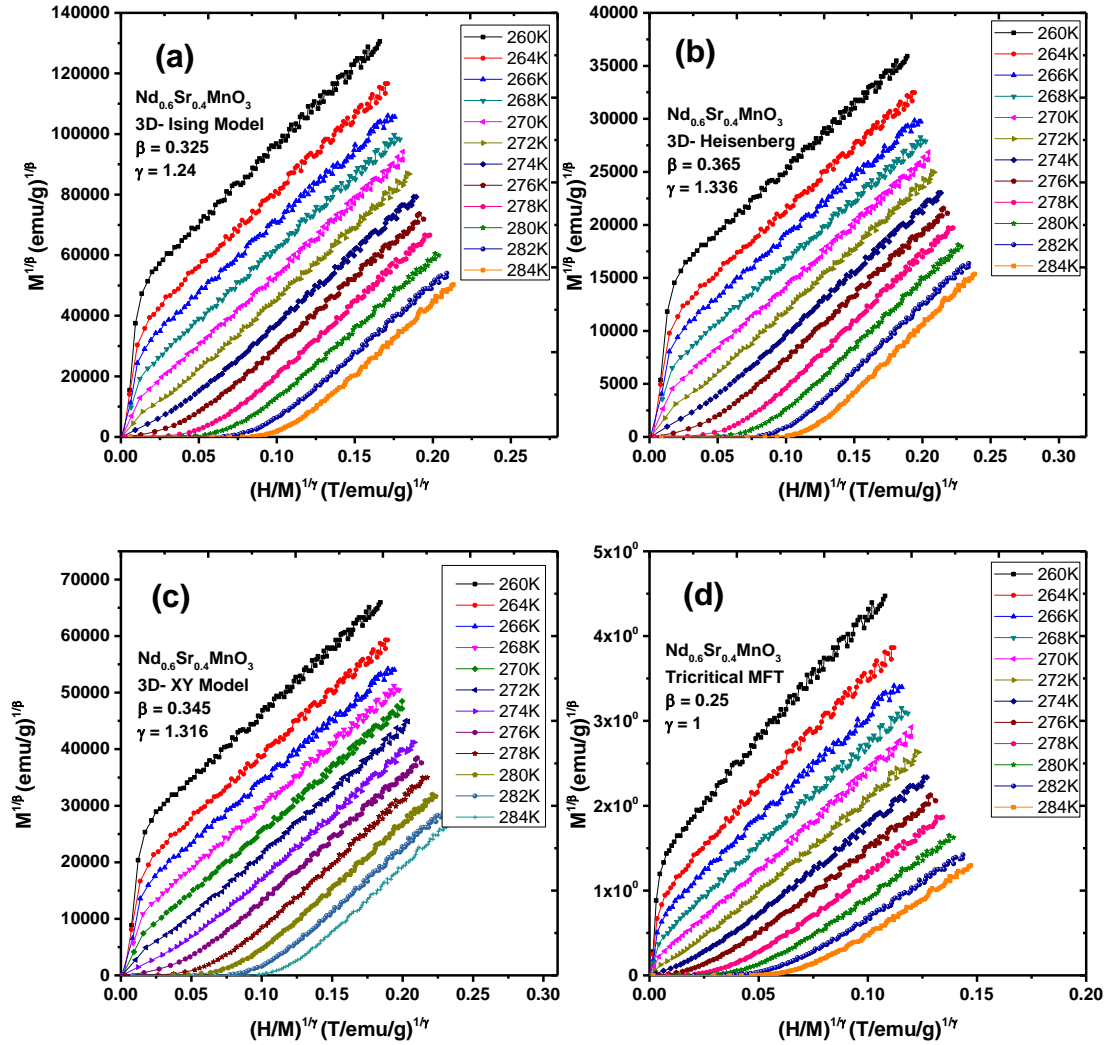


Figure 8: Modified Arrott-plots for $\text{Nd}_{0.6}\text{Sr}_{0.4}\text{MnO}_3$ compound using different models; (a) 3D-Ising model, (b) 3D-Heisenberg model, (c) 3D-XY model, and (d) Tricritical mean field model.

To estimate the experimental values of the critical exponents we used the high field (~4Tesla) magnetic isotherms to obtain the spontaneous magnetization $M_s(T)$ and the initial susceptibility $\chi_0^{-1}(T)$. The 3D-Heisenberg critical exponents for $x=0.00$ and the mean field critical exponents for the Ni-substituted samples $x \geq 0.05$ samples have been used in the modified Arrott (MAP) plot representation. The variations of $M_s(T)$ and $\chi_0^{-1}(T)$ are presented in Fig. 10 (a and b) for $x=0.00$ and 0.05 respectively.

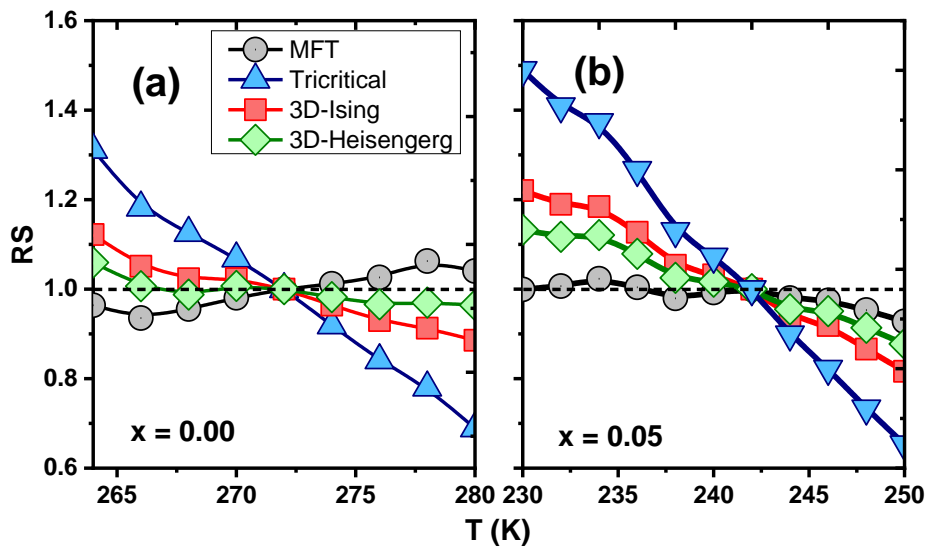


Figure 9: Relative slope (RS) of (a) $x = 0.00$, and (b) $x = 0.05$ sample as a function of temperature defined as $RS = S(T) / S(T_c)$.

The values of critical exponents β , and γ were obtained by fitting the experimental data with $M_s = m_0 |\varepsilon|^\beta$; when $T < T_c$ and $\chi_0^{-1} = \frac{h_0}{m_0} |\varepsilon|^\gamma$; when $T > T_c$ where $\varepsilon = \frac{T - T_c}{T_c}$ is the reduced temperature, m_0 , and h_0 are the critical amplitudes. The critical exponents obtained from the MAP along with T_c for all samples are shown in Table 4. The experimental value of the critical isotherm exponents δ for the Ni-free sample was obtained using the “critical” magnetic isotherm at T_c . The results ($x=0.00$) are presented in figure 11 as $\ln(M)$ vs $\ln(H)$ as shown in figure 11. The

δ value for the Ni substituted sample have been obtained using similar procedure. The results are given in Table 4, which clearly reveals that δ values are lower than the Ni-free sample.

Table 4: Critical exponents $\beta, \gamma,$ and δ for $Nd_{0.6}Sr_{0.4}Mn_{1-x}Ni_xO_3$ compound.

X	Technique	$T_C(K)$	β	γ	δ
0.0	MAP	272.65 ± 0.54	0.314 ± 0.010	1.34 ± 0.07	4.7
	K-F analysis	273.62 ± 0.43	0.357 ± 0.025	1.334 ± 0.048	
0.05	MAP	246.07 ± 0.72	0.40 ± 0.01	1.05 ± 0.01	3.1
	K-F analysis	247.63 ± 0.38	0.49 ± 0.03	1.02 ± 0.01	
0.10	MAP	207.12 ± 0.35	0.47 ± 0.11	0.89 ± 0.05	2.9
	K-F analysis	206.45 ± 0.39	0.44 ± 0.15	0.82 ± 0.05	
0.15	MAP	152.12 ± 0.02	0.43 ± 0.04	0.99 ± 0.02	3.3
	K-F analysis	152.67 ± 0.19	0.36 ± 0.32	0.83 ± 0.06	
0.20	MAP	104.9 ± 0.24	0.40 ± 0.04	1.02 ± 0.14	3.1
	K-F analysis	103.64 ± 0.20	0.48 ± 0.02	1.03 ± 0.05	

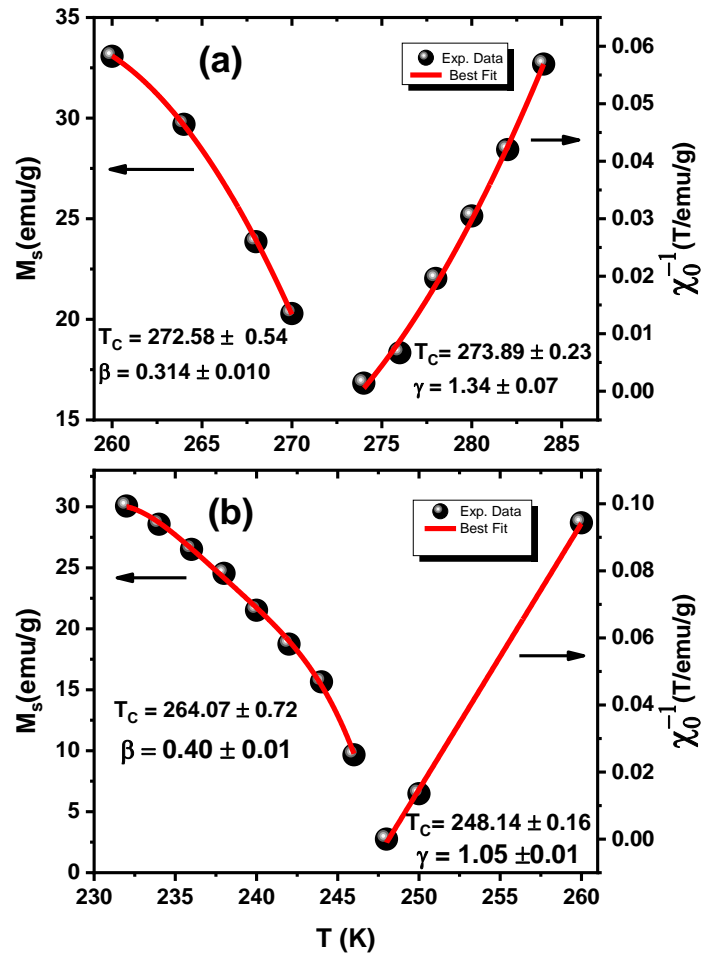


Figure 10: Temperature dependence of $M_s(T)$ and χ_0^{-1} determined from the modified Arrott plot for (a) $x = 0.00$, and (b) $x = 0.05$.

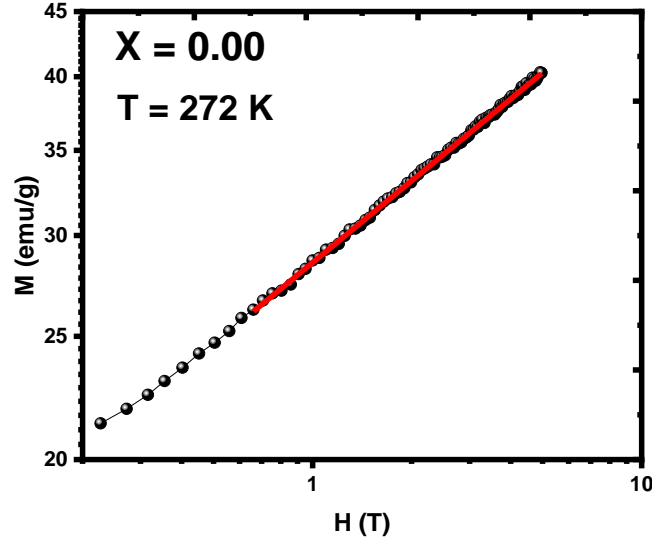


Figure 11: Critical isotherm at $T=T_c$ in the $Nd_{0.6}Sr_{0.4}MnO_3$ compound in log-log scale.

3.4 The Kouvel–Fisher Plot

Kouvel–Fisher (KF) suggested a more precise method to determine the critical exponents [10]. The method is based on linearizing the two main order parameters; M_s and χ_0^{-1} near T_c using the following relations [10]:

$$\frac{M_s(T)}{dM_s(T)/dT} = \frac{T-T_c}{\beta} \quad (2)$$

$$\frac{\chi_0^{-1}}{d\chi_0^{-1}/dT} = \frac{T-T_c}{\gamma} \quad (3)$$

The slopes are: $1/\beta$ and $1/\gamma$, respectively. The KF-plot is illustrated in Fig.12 for both $x = 0.00$ and $x = 0.05$ samples. For the $Nd_{0.6}Sr_{0.4}MnO_3$, the obtained critical exponents are ($\beta = 0.357 \pm 0.025$) and $\gamma = 1.334 \pm 0.048$ which are slightly different from the theoretical values used in the modified Arrott plots. For samples with $x \geq 0.05$, the critical exponents' β and γ are very close

to the mean field value. The critical exponents obtained from the MAP as well as the KF method along with T_C are shown (for all samples) in Table 4 along with the calculate δ values [29].

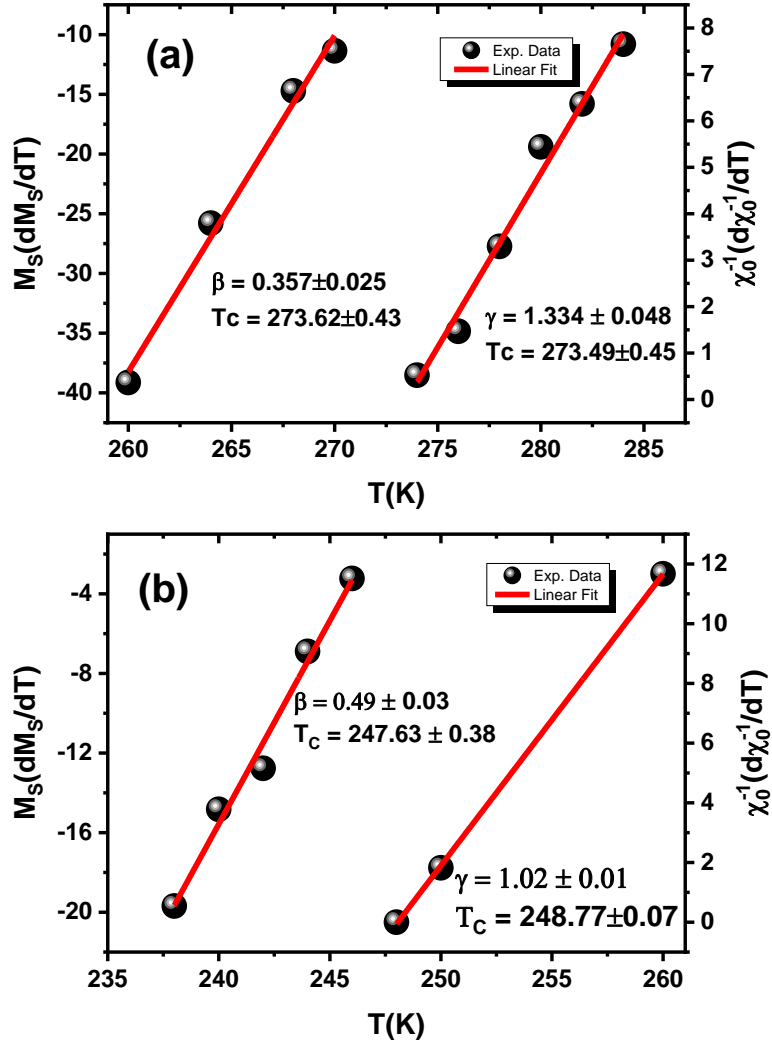


Figure 12: Kouvel-Fisher plots for $M_s(T)$ and χ_0^{-1} plot of (a) $x = 0.00$, and (b) $x = 0.05$.

3.5 Scaling Analysis

Near the critical region the magnetic equation of state can be written as:

$$M(H, \varepsilon) = |\varepsilon|^\beta f_\pm \left(\frac{H}{|\varepsilon|^{\beta+\gamma}} \right) \quad (4)$$

where f_+ is the state function above T_c ($T > T_c$) and f_- is the state function below T_c ($T < T_c$), define ε both are polynomial functions [16]. The renormalized magnetization is defined as $m \equiv |\varepsilon|^{-\beta} M(H, \varepsilon)$, and renormalized field as $h \equiv H|\varepsilon|^{-(\beta+\gamma)}$. This means, Eq. 4 can be rewritten as

$$m = f_{\pm}(h) \quad (5)$$

For the correct values of the critical exponents, β, γ and δ ; Eq. 5 will generate two distinct curves in $M/|\varepsilon|^{\beta}$ vs. $H/|\varepsilon|^{(\beta+\gamma)}$ representation: one curve for T above T_c and another below T_c [28]. Both curves approach each other asymptotically at $T=T_c$. This is an important criterion for critical regime. The scaled data is represented in Fig.13 a and b for $x=0.0$ and 0.05 respectively. All data at various temperatures fall on two distinct curves; one above T_c and the other below T_c . Both curves merge at $T=T_c$. These findings confirm that the obtained values of the critical exponents and critical temperatures are reliable and consistent with the scaling hypothesis.

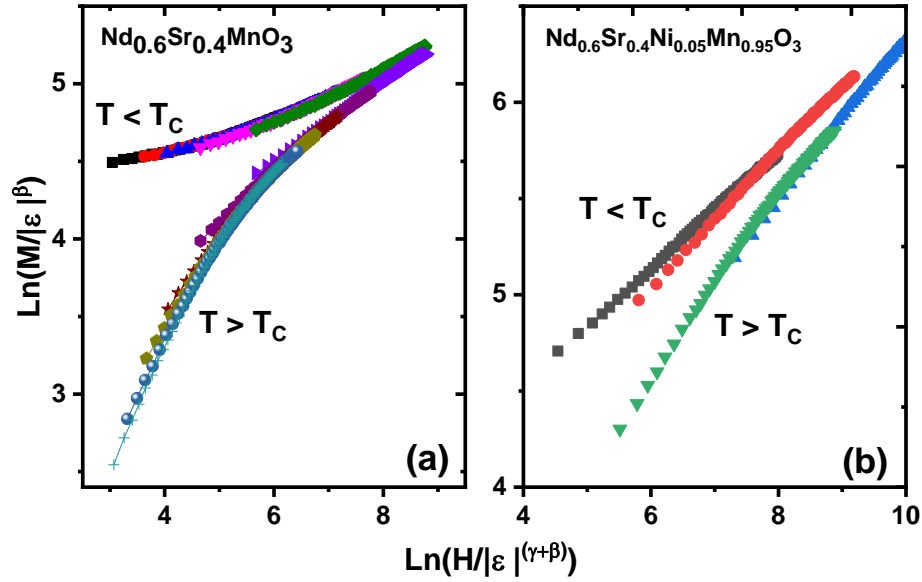


Figure 13: Scaling plots indicating two universal curves below and above T_c for $x=0.00$ and $x=0.05$.

CONCLUSION

The XRD patterns of $\text{Nd}_{0.6}\text{Sr}_{0.4}\text{Mn}_{1-x}\text{Ni}_x\text{O}_3$ with $0.00 \leq x \leq 0.2$ revealed that the major phase in all samples is in the orthorhombic structure with space group $Pnma$. The lattice parameters and the unit cell volume are found to decrease linearly with increasing Ni concentration. Moreover, the angle $O2-Mn-O2$ decreases monotonically with increasing Ni concentration. The critical properties of these perovskite manganites have been studied using the dc magnetization near T_c , using the modified Arrott plot, Kouvel-Fisher method, critical isotherm and scaling analysis. The critical exponents for $x = 0.00$ sample closely follow a 3D Heisenberg model, while the Ni-substituted samples tend to be mean field like model.

The experimental results showed a second-order phase transition. The obtained critical exponents are found to produce a universal scaling of the magnetization data that falls into two distinct curves

below and above the critical temperature. This confirms the reliability of the obtained critical exponents and T_c .

ACKNOWLEDGMENTS

The project has been supported by King Fahd University of Petroleum and Minerals DSR project No. IN121002. The support of the Center of Research Excellence in Nanotechnology (CENT) at KFUPM is gratefully appreciated.

REFERENCES

- [1] Tokura, Y., Nagaosa, N., *Science* 21 Apr 2000, Vol. 288, 5465, pp. 462-468
- [2] Goodenough, J.B.: *Prog. Solid State Chem.* 5, 145 (1972).
- [3] Wang, H., Zhang, X., Hundley, M.F., Thompson, J.D., Gibbons, B.J., Lin, Y., Arendt, P.N., Foltyn, S.R., Jia, Q.X., MacManus Driscoll, J.L.: *Appl. Phys. Lett.* 84, 1147 (2004).
- [4] Ben Jemaa, F., Mahmood, S.H., Ellouze, M., Halouani, F.: *Ceramics International* 41, 8191 (2015).
- [5] Kajimoto, R., Yoshizawa, H., Kawano, H., Kuwahara, H., Tokura, Y., Ohoyama, K., Ohashi, M., *Phys. Rev. B* 60, 9506 (1999).
- [6] Phan, M.H., Yu, S.C., Review of the magnetocaloric effect in manganite materials, *J.Magn. Mater.* 308(2007)325–340.
- [7] Hamad, M. Kh, Developing near room temperature magnetocaloric materials, Morad Hamad, Ph.D. Dissertation, King Fahd University of Petroleum and Minerals (2018).
- [8] Zarai, E., Issaoui, F., Tozri, A., Hussein, M., Dhahri, E.: *J Supercond Nov Magn* (2016) 29:869–877.

- [9] Arrott, A., Noakes, J.E.: Phys. Rev. Lett. 19, 786 (1967).
- [10] Kouvel, J.S., Fisher, M.E.: Phys. Rev. B 136, A1626 (1964).
- [11] Kajimoto, R. Yoshizawa, H. Kawano, H. Kuwahara, H. Tokura, Y. Ohoyama, K. Ohashi, M. Phys. Rev. B 60, 9506 – Published 1 October 1999.
- [12] Venkatesh, R., Pattabiraman, M., Sethupathi, K., Rangarajan, G., Angappane, S., and Park, J.-G. Journal of Applied Physics 103, 07B319 (2008).
- [13] Mansour A.I. Ziq Kh. Salem A.F. · Hamam R.; J Supercond Nov Magn, 27, (2014) 183-186.
- [14] <http://jp-minerals.org/vesta/en/>
- [15] <http://www.crystalimpact.com/diamond/>
- [16] Roisnel, T., Rodriguez-Carvajal, J., Computer program FULLPROF, LLBLCSIM, (2003).
- [17] Young, R.A., The Rietveld Method., International Union of Crystallography Monographs on Crystal.
- [18] Georg Will, Powder Diffraction: The Rietveld Method and the Two Stage Method to Determine and Refine Crystal Structures from Powder Diffraction Data.
- [19] Abdel-Latif A., Ahmed A. M., Mohamed H. F., Saleh S. A., Paixão J. A., Ziq Kh A., Hamad M. Kh., Al-Nahari E G, Ghoza M., Allam S., J. Magn. Magn. Mater. 457, (2018), 126-134.
- [20] Hamad M Kh , Abdel-Latif I A, and Ziq Kh A. IOP Conf. Series: Journal of Physics: Conf. Series 869 (2017) 012032.
- [21] Ahrens, L. H., Geochim. Cosmochim, 2, I55, (1952).
- [22] Shannon R.D., Acta Crystallogr., Sect. A: Found. Crystallogr., 32, 751 (1976).

- [23] Guilherme Oliveira Siqueira, Rose Marie Belardi, Pedro Hespanha Almeida, Charles Luís da Silva, Márcia Caldeira Brant, Tulio Matencio, Rosana Zacarias Domingues. *Journal of Alloys and Compounds* 521 (2012) 50–54.
- [24] Remović-Langer, K., *Magnetic characteristics of metal organic low-dimensional quantum spin systems at low temperatures..PhD Dissertation. der Johann Wolfgang Goethe-Universität*, page 38, (2010).
- [25] Banerjee, S. K., *Phys. Lett.* 12, 16 (1964).
- [26] Huang, K., *Statistical Mechanics*, 2nd ed. Wiley, New York (1987).
- [27] Kaul, S. N., *J. Magn. Magn. Mater.* 53,5 (1985).
- [28] Fan, J., Ling, L., Hong, B., Zhang, L., Pi, L., and Zhang, Y. *Phys. Rev. B* 81, 144426, (2010).
- [29] Widom, B., *J. Chem. Phys.* 43, 3892 (1965).